J. Fluid Mech. (1991), *vol.* 224, *pp.* 133–158
Printed in Great Britain

Three-dimensional simulations of large eddies in the compressible mixing layer

By N. D. SANDHAM[1] AND W. C. REYNOLDS[2]

[1] DLR, Institute for Theoretical Fluid Mechanics, Göttingen, Germany
[2] Stanford University, Stanford, CA 94305, USA and NASA Ames Research Center,
Moffett Field, CA 94035, USA

(Received 24 January 1990 and in revised form 6 August 1990)

The effect of Mach number on the evolution of instabilities in the compressible mixing layer is investigated. The full time-dependent compressible Navier–Stokes equations are solved numerically for a temporally evolving mixing layer using a mixed spectral and high-order finite difference method. The convective Mach number M_c (the ratio of the velocity difference to the sum of the free-stream sound speeds) is used as the compressibility parameter. Simulations with random initial conditions confirm the prediction of linear stability theory that at high Mach numbers ($M_c > 0.6$) oblique waves grow more rapidly than two-dimensional waves. Simulations are then presented of the nonlinear temporal evolution of the most rapidly amplified linear instability waves. A change in the developed large-scale structure is observed as the Mach number is increased, with vortical regions oriented in a more oblique manner at the higher Mach numbers. At convective Mach numbers above unity the two-dimensional instability is found to have little effect on the flow development, which is dominated by the oblique instability waves. The nonlinear structure which develops from a pair of equal and opposite oblique instability waves is found to resemble a pair of inclined Λ-vortices which are staggered in the streamwise direction. A fully nonlinear computation with a random initial condition shows the development of large-scale structure similar to the simulations with forcing. It is concluded that there are strong compressibility effects on the structure of the mixing layer and that highly three-dimensional structures develop from the primary inflexional instability of the flow at high Mach numbers.

1. Introduction

The effect of compressibility on transition and turbulence in the two-stream mixing layer is the subject of much current research, prompted by the proposed development of propulsion systems based on supersonic combustion. The limiting process in such devices is believed to be the time taken to mix fuel and oxidizer in supersonic free shear layers. In this paper we consider the effect of compressibility on a plane mixing layer which is a prototype free shear layer, amenable to study by experiment and numerical simulation.

Early experiments (summarized by Birch & Eggers 1973) showed that the mixing-layer growth rate $\mathrm{d}\delta/\mathrm{d}x$ (δ is a measure of mixing-layer width and x is the streamwise coordinate) was strongly reduced as the Mach number increased. Brown & Roshko (1974) showed that this reduction in growth rate was not due to the effects of density ratio, and hence that a true compressibility effect was being observed. A dimensionless Mach number has been introduced by Bogdanoff (1983) and by

Papamoschou & Roshko (1986, 1988) which appears to collapse the available experimental data onto a single curve of growth rate against Mach number. Following the nomenclature of Papamoschou & Roshko (1988) we call the compressibility parameter the convective Mach number M_c, defined by

$$M_c = \frac{U_1 - U_2}{c_1 + c_2}, \tag{1}$$

where U_1 and U_2 are the free-stream velocities, c_1 and c_2 are the free-stream sound speeds and we assume that the ratio of specific heats γ is constant. For an explanation of the physical arguments behind (1) the reader is referred to Papamoschou & Roshko (1988). However, we should note that recent measurements of the convective velocities of organized structures in the compressible mixing layer (Papamoschou 1989) call into question some of these physical arguments. Further investigation is this area is needed. For the purpose of this paper we take (1) as a simple dimensionless Mach number that collapses the available experimental growth-rate data.

Recent experiments have begun to document the large-scale structure of the compressible mixing layer. Clemens *et al.* (1990) showed how integrated methods such as schlieren can give a false impression of two-dimensionality in the mixing layer at $M_c = 0.6$. In a continuation of this work Clemens & Mungal (1990) compared the structure at three separate convective Mach numbers. They found a two-dimensional 'roller' structure at $M_c = 0.28$, while at $M_c = 0.62$ and 0.79 the flow was much more three-dimensional.

Numerical work on the compressible mixing-layer problem began with solutions of the linear stability problem. Lessen, Fox & Zien (1965, 1966) solved the temporal stability problem. They found compressibility to be stabilizing and also found 'supersonic' modes of instability (modes with a phase speed supersonic relative to one or other of the free streams) at high Mach numbers. Gropengiesser (1969) solved the spatial stability problem for realistic base profiles of velocity and temperature and noted the strong amplification rate of oblique instability waves at high Mach numbers. Recent stability calculations have shown that the convective Mach number can to first order collapse the linear stability results, and that when one plots the spatial amplification rate of the most amplified instability wave (including oblique waves) one obtains a growth rate against convective Mach number curve very similar to the experiments (Ragab & Wu 1988; Sandham & Reynolds 1990).

Two-dimensional simulations of the compressible Navier–Stokes equations for the compressible mixing layer have been presented a number of times. These simulations (for example Lele 1989; Sandham & Reynolds 1989) show a strong reduction in mixing-layer growth rate as Mach number is increased. Above approximately $M_c = 0.7$ the simulations show the development of weak shock waves, situated around the large-scale two-dimensional vortices that develop from the instability in the flow. The limitation of these simulations is clearly the imposed two-dimensionality, especially since at the higher Mach numbers linear stability theory predicts that oblique waves are more rapidly amplified than two-dimensional waves.

Two-dimensional simulations of the wall-bounded free shear layer have been presented by Eberhardt *et al.* (1988) and by Greenough *et al.* (1989). In this case there can be many extra instability modes of the 'acoustic' variety, similar to those found in the compressible boundary-layer problem (Mack 1984). The simulations to date have not shown any vortex roll-up developing from these instability modes, and hence no enhanced mixing capability. A linear stability analysis of the wall-bounded

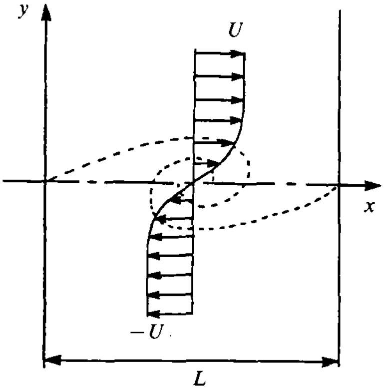

FIGURE 1. Schematic of the time-developing mixing layer.

shear layer problem has recently been presented by Zhuang *et al.* (1990). The results appear to show that even the most unstable wall modes are less unstable than the oblique (subsonic) modes from the unbounded problem, though the authors do not comment on this.

In this paper we consider the nonlinear evolution of the key three-dimensional instability waves in the unconfined mixing layer. The objective is to identify the important physical effects of compressibility, in particular on the large-scale structure which develops from the primary instability in the flow. The method is a full time-dependent, three-dimensional solution of the Navier–Stokes equations. We begin with an overview of the numerical method and the key results from linear stability theory, and then proceed to simulations of the effects of Mach number on the nonlinear evolution of various combinations of instability waves. The generality of the results is checked by performing simulations with random initial conditions.

2. Governing equations

The computational domain for the time-developing mixing layer is shown on figure 1. The flow is periodic in the streamwise direction (x) and in the spanwise direction (z) (out of the page). The flow is unbounded in the normal (y) direction.

We begin by defining a non-dimensionalization scheme,

$$u_i = \frac{u_i^*}{U_1^*}, \quad \rho = \frac{\rho^*}{\rho_1^*}, \quad p = \frac{p^*}{\rho_1^* U_1^{*2}}, \quad T = \frac{T^*}{T_1^*}, \tag{2a}$$

$$\mu = \frac{\mu^*}{\mu_1^*}, \quad e = \frac{e^*}{U_1^{*2}}, \quad t = \frac{t^* U_1^*}{\delta_{\omega_0}^*}, \quad x_i = \frac{x_i^*}{\delta_{\omega_0}^*}, \tag{2b}$$

where x_i are the Cartesian coordinates (x,y,z), t is the time, u_i are the velocity components (u,v,w), ρ is the density, p the pressure, T the temperature, μ the viscosity and e the internal energy per unit mass. The superscript * refers to a dimensional quantity and the subscript 1 refers to the upper ($y > 0$) free stream. The reference lengthscale is $\delta_{\omega_0}^*$, the vorticity thickness of the initial velocity profile,

$$\delta_{\omega_0}^* = \frac{U_1^* - U_2^*}{|\mathrm{d}\bar{u}_0^*/\mathrm{d}y^*|_{\max}}, \tag{3}$$

where $\bar{u}_0^*$ is the specified initial mean streamwise velocity profile.

Using this non-dimensional scheme the governing equations for continuity, momentum and energy become (Anderson, Tannehill & Pletcher 1984):

$$\frac{\partial \rho}{\partial t}=-\frac{\partial(\rho u_i)}{\partial x_i}, \tag{4}$$

$$\frac{\partial(\rho u_i)}{\partial t}=-\frac{\partial(\rho u_i u_j+p\delta_{ij})}{\partial x_j}+\frac{\partial \tau_{ij}}{\partial x_j}, \tag{5}$$

$$\frac{\partial E_{\mathrm{T}}}{\partial t}=-\frac{\partial[(E_{\mathrm{T}}+p)\,u_i]}{\partial x_i}-\frac{\partial q}{\partial x_i}+\frac{\partial(u_j\tau_{ij})}{\partial x_i}, \tag{6}$$

where the total energy $E_{\mathrm{T}}=\rho(e+\frac{1}{2}u_i u_i)$. The non-dimensional constitutive relations for a Newtonian fluid with Fourier heat conduction are:

$$\tau_{ij}=\frac{\mu}{Re}\left(\frac{\partial u_i}{\partial x_j}+\frac{\partial u_j}{\partial x_i}-\frac{2}{3}\frac{\partial u_k}{\partial x_k}\delta_{ij}\right), \tag{7}$$

$$q_i=\frac{-\mu}{(\gamma-1)M_1^2 Pr Re}\frac{\partial T}{\partial x_i}, \tag{8}$$

where M_1 is the Mach number of the upper $(y>0)$ free stream $M_1=U_1^*/c_1^*$.

The Reynolds number of the flow is defined by $Re=\rho_1^* U_1^* \delta_{\omega_0}^*/\mu_1^*$, and the Prandtl number by $Pr=c_p^*\mu^*/k^*$, where k^* is the thermal conductivity. The viscosity is assumed to follow a power law, non-dimensionally $\mu=T^{0.67}$, where we have chosen the exponent for nitrogen (White 1974). The perfect-gas law in our non-dimensional scheme is

$$p=\frac{\rho T}{\gamma M_1^2}=\rho(\gamma-1)\,e. \tag{9}$$

In all the simulations a passive scalar equation is also solved. The non-dimensional equation for a scalar f is

$$\frac{\partial(\rho f)}{\partial t}=-\frac{\partial(\rho f u_i)}{\partial x_i}+\frac{1}{ReSc}\frac{\partial}{\partial x_i}\left(\mu\frac{\partial f}{\partial x_i}\right), \tag{10}$$

where the Schmidt number $Sc=\mu^*/\rho^* D^*$ (D^* is a diffusion coefficient) is assumed to be constant. The quantity ρf can be thought of as the concentration per unit volume of a trace species.

In all the computations we take the Prandtl number to be constant $Pr=1$ and the Schmidt number $Sc=1$.

3. Numerical methods

We present a direct numerical simulation of the time-developing mixing-layer problem. That is to say, we solve the governing equations in their entirety, with no turbulence model. In order to resolve the flow features we use spectral and high-order-accurate finite-difference methods.

Time-advance of the computational variables (ρ, ρu_i, E_{T} and ρf) is obtained by a fully explicit compact-storage Runge–Kutta method (Wray 1986). The right-hand sides of the equations for these variables (equations (4), (5), (6) and (10)) require the evaluation of derivatives of various quantities. Derivatives in the periodic directions x and z are readily obtained with a simple Fourier method: fast Fourier transform, multiply by ik, where k is the wavenumber, and inverse transform. Derivatives in the non-periodic y-direction are obtained with a sixth-order modified Padé scheme (Lele 1990). In the y-direction we prefer not to attempt a solution on an infinite domain, since we would not be able to resolve sound waves in the free stream. The method adopted here is to chop the computational domain at some y-location and impose non-reflecting boundary conditions. The basic idea of these boundary conditions, which were developed by Thompson (1987), is to consider the characteristic form of the Euler equations at the boundary. Outgoing characteristics use information from within the computational domain, and hence can be computed without manipulation. Incoming characteristics are handled by setting the time-derivative of their amplitude equal to zero, thus giving the boundary conditions their non-reflecting character. Details of the algorithmic implementation can be found in Sandham & Reynolds (1989), together with results from validation tests.

During the course of our work various other numerical methods were implemented and tested. Initially it was considered likely that shock waves would form at the higher Mach numbers, so a class of 'shock-capturing' numerical methods were investigated. Results from evaluation of these schemes, together with a simple MacCormack method, can be found in Sandham & Yee (1989). When it became apparent that shock waves were not a feature of the flow in three-dimensions at high Mach number, it was decided to sacrifice the shock-capturing capability and concentrate instead on the high spatial accuracy of the above scheme.

The time-developing mixing layer develops from specified initial conditions. In these computations we use a simple error function as the base velocity profile:

$$\bar{u}_0 = \operatorname{erf}(y\pi^{\frac{1}{2}}) \tag{11}$$

The initial mean temperature profile can be specified as a solution to the compressible boundary-layer energy equation (White 1974), assuming unity Prandtl number. For the antisymmetric mean velocity profile considered here, and with equal free-stream temperatures the general relation (see e.g. Sandham & Reynolds 1989) reduces to

$$\bar{T}_0 = 1+M_1^2\frac{\gamma-1}{2}(1-\bar{u}_0^2). \tag{12}$$

It is noted that for all the simulations presented here the convective Mach number M_c is equal to the free-stream Mach number M_1. Uniform pressure is assumed for the initial mean flow ($\bar{p}_0 = 1$), so the mean density profile is readily obtained from (9). Superimposed on the mean profiles are disturbances, which are either random noise or combinations of eigenfunctions from the linear stability analysis. The particular disturbances are described in later sections. The Reynolds and Mach numbers are specified for each simulation separately.

The simulations were typically begun on a small (x, y, z) mesh of $(16 \times 99 \times 16)$, since relatively few Fourier modes are required in x and z to resolve the linear and slightly non-linear growth of the instabilities. As the flow became more nonlinear the number of Fourier modes in x and z was increased, with the mesh ending typically at $(96 \times 99 \times 96)$. The upper limit on the mesh size was fixed by the available storage on the Cray X-MP computer and by the amount of computer time (10–15 h) that we were prepared to expend per simulation. The full number of points were required in the y-direction from the start of the simulation, in order to resolve the eigenfunctions.

4. Linear stability theory

Linear stability theory was used to provide eigenfunctions of unstable waves, which were then used as initial conditions for the numerical simulations. It was also used to guide the choice of M_c and Re for the simulations. In this section we give an overview of the results from inviscid temporal linear stability analysis of the time-developing mixing layer. Similar physical characteristics were found in the inviscid spatial stability analysis of the spatially developing mixing layer (Sandham & Reynolds, 1989, 1990).

A parallel mean flow is assumed and the decomposition $u = \bar{u} + u'$ is used (similarly for v', w', ρ' and T'). Solutions to the linear equations have the form:

$$u' = \hat{u}e^{i(\alpha x + \beta z - \omega t)}, \tag{13}$$

where α and β are wavenumbers in the x- and z-directions respectively and ω is the disturbance frequency. The eigenfunction $\hat{u}$ is a function of the y-coordinate only. For the time-developing mixing-layer problem disturbances grow in time and not in space. Thus, the wavenumbers α and β are real quantities. The streamwise wavelength of a disturbance is given by $L_x = 2\pi/\alpha$, the phase speed by $c_r = \omega_r/\alpha$, and the amplification rate by ω_i.

At low Mach numbers (for $M_c < 0.6$) the two-dimensional disturbance $\theta = 0°$ (where $\tan\theta = \beta/\alpha$) is the most unstable wave. The effect of M_c on the growth rate ω_i of two-dimensional waves is shown on figure 2(*a*). It can be seen that the amplification rate of these waves is strongly reduced as M_c increases. By $M_c = 1.2$ the maximum amplification rate for two-dimensional waves is only 10% of its incompressible value.

In the time-developing mixing layer, with an antisymmetric mean velocity profile and equal free-stream temperatures, the phase speed of the subsonic instability waves is zero. This can be seen from the plot of ω_r on figure 2(*b*). Above $M_c = 1$ we observe the presence of two new 'supersonic' instability waves, i.e. waves with a phase speed that is supersonic relative to one or other of the free streams. These waves are the most unstable waves *in two dimensions* above a convective Mach number of approximately 1.0. Numerical simulations of these waves (Sandham & Reynolds 1989) showed that the very small growth rates of these instabilities persisted in the nonlinear regime of disturbance growth.

The linear stability picture is especially interesting in three dimensions. The amplification rate of unstable waves at various Mach numbers as a function of wave angle θ is shown on figure 3. The most unstable wave was found for each M_c as a function of α and θ. To produce the curves, the wavelength was fixed at that of the most unstable wave and the angle θ was varied. The curves split into two regimes: for $M_c < 0.6$ the two-dimensional instability wave is the most unstable wave, whilst for $M_c > 0.6$ an oblique wave is most unstable. It was found (Sandham & Reynolds, 1989, 1990) that, especially for the case of equal free-stream temperatures, the angle of the most unstable inviscid linear instability wave above $M_c = 0.6$ satisfied

$$M_c \cos\theta \approx 0.6. \tag{14}$$

Thus the obliquity of the most unstable wave increases as the Mach number increases.

Large-scale structure in free-shear layers is intimately connected with the underlying instability of the flow. Brown & Roshko (1974) demonstrated that organized structure in the incompressible mixing layer persisted up to high Reynolds

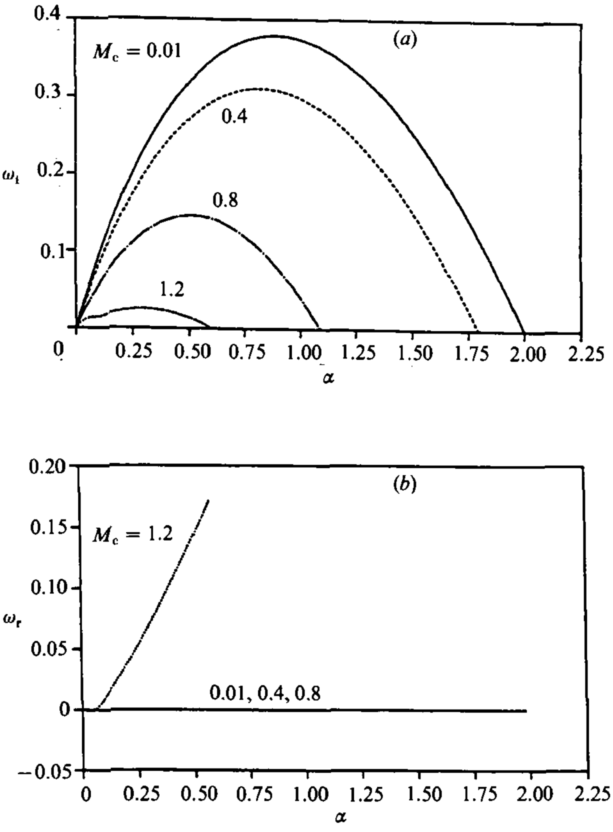

FIGURE 2. The eigenvalue from inviscid temporal linear stability analysis: (*a*) ω_i, (*b*) ω_r.

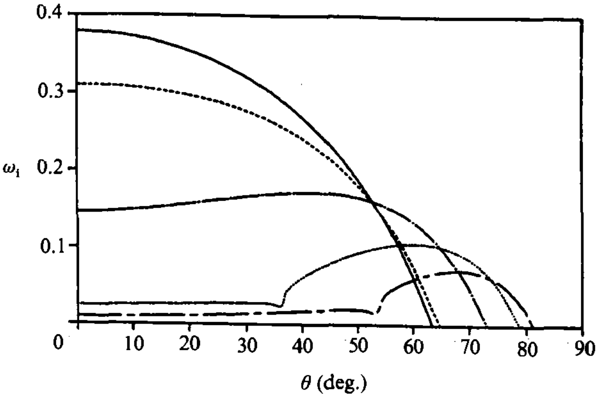

FIGURE 3. Temporal inviscid linear growth rate ω_i as a function of wave angle θ. —, $M_c = 0.01$, $\alpha = 0.89$; ----, $M_c = 0.4$, $\alpha = 0.82$; —·—, $M_c = 0.8$, $\alpha = 0.52$; ·····, $M_c = 1.2$, $\alpha = 0.315$; —, $M_c = 1.6$, $\alpha = 0.22$.

numbers, even when the flow was statistically self-similar. Hence, the organized structures were not simply a remnant of the transition process. The primary structure observed in Brown & Roshko's photographs is a large two-dimensional roller, consistent with the underlying infexional (inviscid) instability of the mean flow, where the most unstable wave is two-dimensional. The inflexional instability

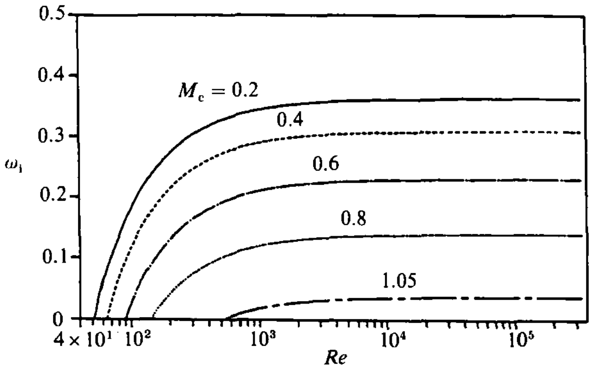

FIGURE 4. Temporal linear growth rate of a fixed disturbance shape (the two-dimensional inviscid eigenfunction) as a function of Reynolds number and Mach number.

has been proposed by Lesieur *et al.* (1988) as a mechanism for recreation of two-dimensionality, even after three-dimensionality has appeared in the incompressible mixing layer. There is evidence for a quantitative relationship between linear stability theory and mixing-layer growth rate (Sandham & Reynolds 1989, 1990). Mungal & Hollingsworth (1989) discuss evidence for organized structure in a different free shear flow, an extremely high Reynolds number jet. They also make the connection between organized structure and the underlying instability of the flow. With these points in mind, we consider a split of the Mach-number range into three approximate regimes with different instability characteristics, and hence probably different physical character and large-scale structure.

(*a*) $0 < M_c < 0.6$: low-Mach-number regime

The two-dimensional instability is the most rapidly amplified disturbance. Towards $M_c = 0.6$ there are a wide range of waves of different orientations that are approximately equally amplified, so a trend towards three-dimensionality is expected.

(*b*) $0.6 < M_c < 1.0$: increasing three-dimensionality

In this range of Mach numbers an oblique wave is the most amplified wave, so the flow might be expected to have a strong three-dimensional character. However, the two-dimensional wave is still amplified and may have an effect.

(*c*) $M_c > 1.0$: oblique mode dominance

In this region the two-dimensional instability is a factor of approximately 5 less rapidly amplified than the most unstable oblique wave, and may be expected to have a minimal effect on the development of the flow. This region extends up to at least $M_c = 3.2$, which was the highest Mach number for which the stability calculations were carried out (Sandham & Reynolds 1989).

To complete this discussion of the growth of small-amplitude disturbances we present a series of three simulations at various M_c, with random initial conditions. The M_c were selected to be 0.4, 0.8 and 1.05, and the respective *Re* were 400, 600 and 800. The choice of *Re* and M_c was influenced by the nature of the linear instability. Figure 4 shows the growth rate of a particular small-amplitude disturbance (the two-dimensional inviscid eigenfunction) as a function of *Re*. The values of the growth rate were obtained by running the full Navier–Stokes code forward one time step and comparing the amplitude of the fundamental Fourier mode with the initial condition.

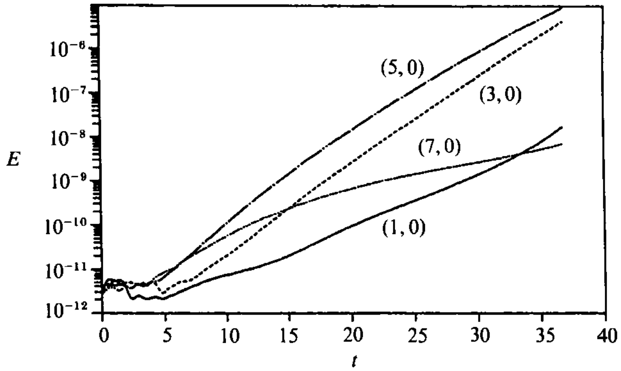

FIGURE 5. Mode energy E as a function of time for a simulation beginning with random initial conditions.

It can be seen from the figure that at higher M_c higher Re are needed in order to reach the asymptotic high-Re region, where we would ideally make our simulations. For this reason we choose higher Re at the higher M_c and limit the highest M_c to 1.05. This means that we are not able to compute so far into the nonlinear regime at higher M_c. The computational box size was chosen to be 40 in both the streamwise and spanwise directions, and 10 in the normal direction. This box size allows approximately 5 of the most unstable waves at $M_c = 0.4$, 3 at $M_c = 0.8$ and 2 at $M_c = 1.05$. The computations were carried out on a $32 \times 33 \times 32$ grid, with an initial seeding of eight complex Fourier modes in x and z. The random noise was added in the following manner (cf. Lesieur *et al.* 1988). For example for the density ρ:

$$\rho(x,y,z) = \rho(x,y,z) + ar\,\mathrm{e}^{-y^2}, \tag{15}$$

where a is the amplitude, chosen to be 0.0001 and r is a random number uniformly distributed between -0.5 and $+0.5$, different for each spatial location, and for each computational variable. The exponential term guarantees that disturbances decay in the free stream.

The simulations were run through the linear region of disturbance growth, and then stopped. We define an energy E as

$$E(k_x, k_z) = \int_{-L_y/2}^{L_y/2} \tilde{u}_i(k_x, k_z)\,\tilde{u}_i^{\dagger}(k_x, k_z)\,\mathrm{d}y, \tag{16}$$

where † indicates a complex conjugate. The k_x and k_z will be taken as integer wavenumbers equal to the number of wavelengths contained in the computational box. For example (3, 0) would be a two-dimensional wave, with wavelength $\frac{1}{3}L_x$. An example of the growth of energy in various modes is shown on figure 5 for the case $M_c = 0.4$. The linearly unstable waves emerge from the background noise at around time $t = 5.0$. In this low-M_c case the (5, 0) mode is the most unstable. These simulations were run at finite Re, so the mean flow thickens during the simulations. This effectively changes the reference lengthscale for the linear instabilities, and leads to the curvature of the modal energies shown on figure 5. The trend is to longer wavelengths being more rapidly amplified at later times in the simulations.

For a simple look at the flow structure that is developing from the linear instabilities, we plot the $v = 0$ contour in the (x, z)-plane at $y = 0$. This contour separates fluid moving up from fluid moving down, and was found to reveal the general nature of the growing instability waves. The result is shown on figure 6 for

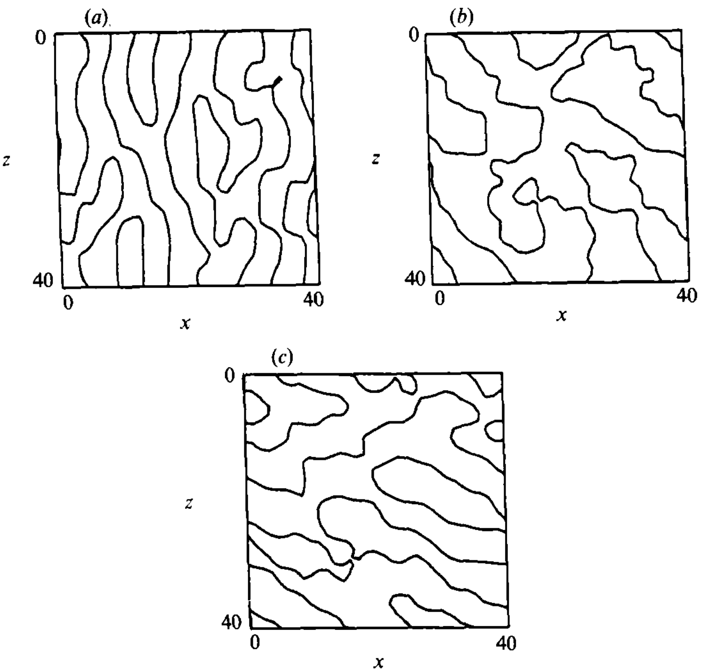

FIGURE 6. The contour $v = 0$ in a cut through the (x, z)-plane at $y = 0$ showing the orientation of instability waves that have grown out of random noise, through the linear region of disturbance growth: (a) $M_c = 0.4$, (b) $M_c = 0.8$ and (c) $M_c = 1.05$.

$M_c = 0.4, 0.8$ and 1.05. At $M_c = 0.4$ (figure 6a) we find a clear preference for spanwise-oriented structures to develop, as is expected from the dominance of the two-dimensional instability at low M_c. At $M_c = 0.8$ (figure 6b) and $M_c = 1.05$ (figure 6c) we observe a different behaviour. The orientation of the contour lines is in agreement with the linear stability theory, which predicts 45° at $M_c = 0.8$ and 60° at $M_c = 1.05$ as the most rapidly amplified waves.

These simulations also give some indication of possibilities for later nonlinear evolution of the flow. For example, at $M_c = 1.05$ (figure 6c) we observe regions in the flow where one oblique wave dominates the other one (a single oblique line results), and regions where the oblique waves have comparable amplitudes (a checkerboard pattern of hills and valleys).

From the above simulations of small-amplitude instability waves developing from random noise we conclude that there is a good qualitative agreement with linear stability theory. No evidence was found for any additional unstable modes, beyond those already known from linear stability analysis.

5. Results from numerical simulations

In this section we consider the effect of convective Mach number on the nonlinear evolution of various combinations of unstable waves. In particular, the temporal development of a combination of a two-dimensional and a pair of oblique waves is considered. The initial condition for such a combination of waves can be written as

$$u' = a_1 \operatorname{Re}\{\hat{u}(\alpha, 0)\, e^{i(\alpha x + \phi)}\} + a_2 \operatorname{Re}\{\hat{u}(\alpha, \beta)\, e^{i(\alpha x + \beta z)} + \hat{u}(\alpha, -\beta)\, e^{i(\alpha x - \beta z)}\}, \qquad (17)$$

with similar perturbations for ρ', v', w' and T'. The disturbance amplitudes are a_1 and a_2. The wavenumber in the streamwise direction is $\alpha = 2\pi / L_x$ and in the spanwise

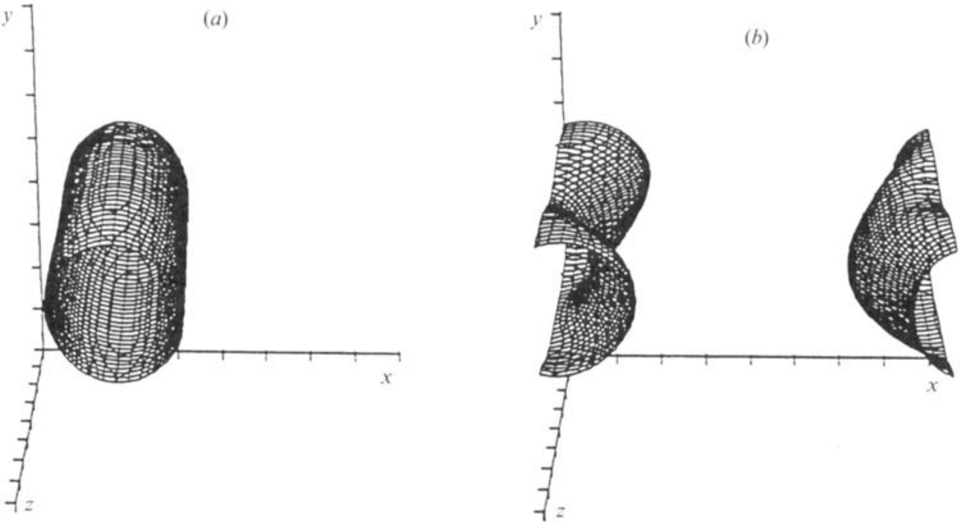

FIGURE 7. Surface of constant pressure, showing the developed large-scale structure at $M_c = 0.4$; (a) bulging mode ($\phi = 0$) and (b) translative mode ($\phi = \frac{1}{2}\pi$).

direction $\beta = 2\pi/L_z$, where L_x and L_z are wavelengths in the x- and z-directions respectively. The eigenfunctions came from the linear stability analysis and were normalized so that the peak magnitude of $\hat{u}$ was 1. The eigenfunction for the two-dimensional wave is $\hat{u}(\alpha, 0)$. For the equal and opposite oblique waves the eigenfunctions are $\hat{u}(\alpha, \beta)$ and $\hat{u}(\alpha, -\beta)$. One need not consider the effect of a phase difference between the equal and opposite oblique waves since such a phase only moves the wave pattern around in space. The important phase is ϕ, the phase difference between the two-dimensional wave and the pair of oblique waves.

Four classes of simulations are described in the following sections. First, simulations of the low-Mach-number mixing layer, to find the combination of instability waves that gives experimentally observed phenomena. Second, forced simulations with a fixed pattern of initial disturbance, to investigate the effect of Mach number on the mixing-layer structure. Third, forced simulations of the combinations of instability waves that are expected to be dominant at the higher Mach numbers, with the objective of identifying possible organized structure at high Mach number. Fourth, a simulation with random initial conditions to check the generality of the results.

5.1. *Low-Mach-number simulations*

The effect of the phase ϕ in (17) was first considered, with the objective of recovering the secondary instabilities of Pierrehumbert & Widnall (1982). Two simulations were run at $M_c = 0.4$, $Re = 400$ with amplitudes $a_1 = 0.05$, $a_2 = 0.025$, and phases $\phi = 0$ and $\frac{1}{2}\pi$. The computational box length was fixed at $L_x = 7.854$, set by the most amplified two-dimensional wave from linear stability theory. There are two considerations behind the choice of L_z. The secondary stability analysis of Pierrehumbert & Widnall suggests 56° as the most unstable secondary instability, though the peak is very broad. However, we initialized our simulations with linear eigenfunctions and the $\theta = 56°$ disturbance, although inviscidly amplified, is initially damped at our Reynolds number. We preferred to have initially growing oblique disturbances, and so chose the compromise value $\theta = 45°$, or $L_x = L_z$. The box size in the normal direction was chosen to be $L_y = 10$.

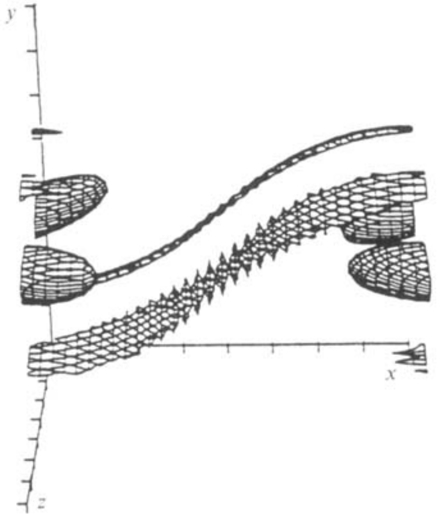

FIGURE 8. Surface of constant streamwise vorticity, showing the stretching of vorticity into braids ($M_c = 0.4$ and $\phi = \frac{1}{2}\pi$).

The particular secondary instability excited by the initial choice of ϕ can be predicted from the eigenfunctions (Sandham & Reynolds 1989). Specifically, $\phi = 0$ excites the 'bulging' mode of instability and $\phi = \frac{1}{2}\pi$ excites the 'translative' mode. The terminology is taken from Pierrehumbert & Widnall (1982). Figure 7 shows surfaces of constant pressure after the nonlinear growth of the instabilities for the two cases, with pressure level chosen as to enclose a region of low-pressure fluid. In all the cases considered in this paper a low-pressure region was associated with rotating fluid. This was checked by examining the passive scalar field, which clearly showed the motion of fluid that originated on one or other side of the mixing layer. Figure 7(*a*) shows the large-scale rotational structure that developed from the simulation of the bulging mode of instability ($\phi = 0$). In this case the core of the spanwise vortex has a diameter that varies sinusoidally in the spanwise direction (recall that the simulations are periodic in x and z). In agreement with Pierrehumbert & Widnall we find that this mode is only weakly amplified. The developed structure is a highly two-dimensional roller. The structure developing from the translative mode of secondary instability ($\phi = \frac{1}{2}\pi$) is shown on figure 7(*b*). This mode is more amplified, and gives a final structure of a vortex core that oscillates, or 'snakes', in the spanwise direction.

A perspective view of a surface of constant streamwise vorticity (figure 8) reveals an important feature of the simulation with $\phi = \frac{1}{2}\pi$: the streamwise vorticity, that was initially placed in the saddle-point region between the vortex cores, has been stretched along the principal axis of strain into long thin regions of vorticity. In our simulations, which all develop from small-amplitude instability waves, there is never enough circulation in these vortical regions to trigger the 'collapse' process (a transition from vorticity into vortices) of Lin & Corcos (1984). The collapse would produce regions of low pressure, which would have shown up on the plot of pressure (figure 7*b*). Rogers & Moser (1989) performed incompressible computations of this phenomenon, and found behaviour similar to that found in our low-Mach-number simulations, when small-amplitude initial disturbances were used. They also reproduced the 'collapse' process of Lin & Corcos when high-amplitude initial disturbances were applied.

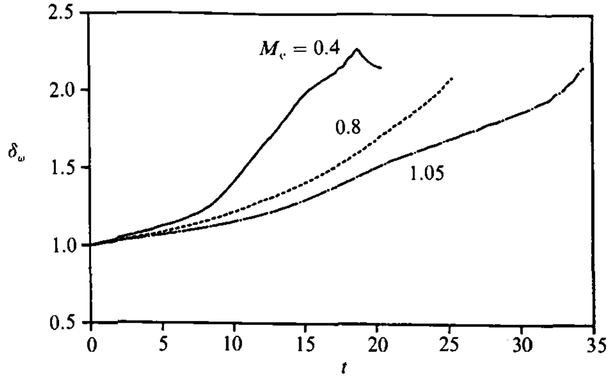

FIGURE 9. Variation of vorticity thickness with time during simulations beginning with a two-dimensional wave and a pair of equal and opposite oblique waves.

The conclusion of these low-Mach-number simulations is that the phase $\phi = \frac{1}{2}\pi$ between a two-dimensional instability wave and a pair of equal and opposite oblique waves reproduces the main secondary instability of the incompressible mixing layer. This phase also places streamwise vorticity in the saddle-point region between successive rollers. Subsequent 'collapse' of this vorticity would give the experimentally observed 'braid' vortices (Bernal & Roshko 1986). Thus, $\phi = \frac{1}{2}\pi$ reproduces most of the important features of the low-Mach-number mixing layer.

5.2. *Effect of Mach number*

For one particular combination of instability waves, we now consider the effect of Mach number. The case of a two-dimensional wave plus a pair of equal and opposite waves with $\phi = \frac{1}{2}\pi$ was selected (see previous section). Convective Mach numbers of 0.4, 0.8 and 1.05 were selected, representative of the three regions of different instability character. At each Mach number the box length L_x was fixed by the most unstable wavelength from linear stability analysis. At $M_c = 0.4$ we have $L_x = L_z = 7.85$, again choosing the $\theta = 45°$ oblique waves (see previous section). At $M_c = 0.8$ we have $L_x = L_z = 13.37$. At this Mach number there is no problem in choosing the $\theta = 45°$ oblique wave, since this is the most unstable wave. At $M_c = 1.05$ we chose $L_x = 18.48$ and $L_z = 12.465$, since a 60° wave is the most unstable linear wave. The box size in the normal direction was selected to be $L_y = 10$. Instability waves were added to the initial condition with $a_1 = a_2 = 0.025$ (see (17)). Reynolds numbers were chosen in the same manner as in the previous section: $Re = 400$ at $M_c = 0.4$, 600 at $M_c = 0.8$ and 800 at $M_c = 1.05$. The simulations were run as far as possible into the nonlinear region, and were stopped when resolution on the finest grids (typically $96 \times 99 \times 96$) became a problem. A plot of the vorticity thickness evolution during the simulations is shown on figure 9. The reduction in growth rate due to compressibility is apparent. However, we still observe strong growth at the highest Mach number considered, contrary to two-dimensional computations (Sandham & Reynolds 1989) which show extremely slow growth at this Mach number. The sharp peak in the vorticity thickness at $t = 18$ ($M_c = 0.4$) is associated with the saturation of the two-dimensional instability mode. However, in other simulations the vorticity thickness was found to be a very sensitive measure of shear-layer thickness that was liable to strong fluctuations, independent of instability mode behaviour.

We next consider the growth of the energy $E(k_x, k_z)$, defined in (16). Plots of E

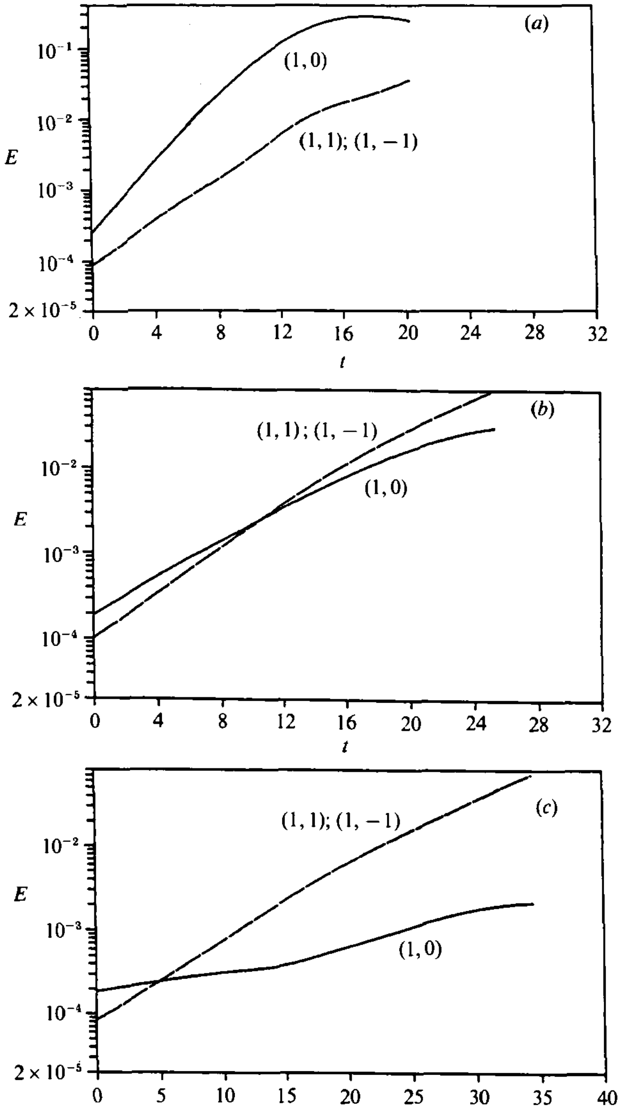

FIGURE 10. Variation of energy E in modes (1, 0) (1, 1) and (1, −1) as a function of time: (a) $M_c = 0.4$, (b) $M_c = 0.8$ and (c) $M_c = 1.05$.

against time during the simulations are shown on figure 10(*a–c*) for each Mach number. We plot the energy in the two-dimensional wave (1, 0) and the two oblique waves (1, 1) and (1, −1). Because of the symmetry in (17) the oblique waves grow at exactly the same rate. At $M_c = 0.4$ (figure 10*a*) it can be seen that the (1, 0) wave is the most rapidly amplified wave initially, and always has more energy than the oblique waves. At $M_c = 0.8$ (figure 10*b*) the oblique waves (1, 1) and 1, −1) are more rapidly amplified than the two-dimensional wave. Although they start with less energy, they soon overtake the (1, 0) wave. At the highest Mach number $M_c = 1.05$ (figure 10*c*) the oblique waves have a much stronger growth rate, and by the last time in the simulation they have an energy content well over an order of magnitude higher than the two-dimensional wave.

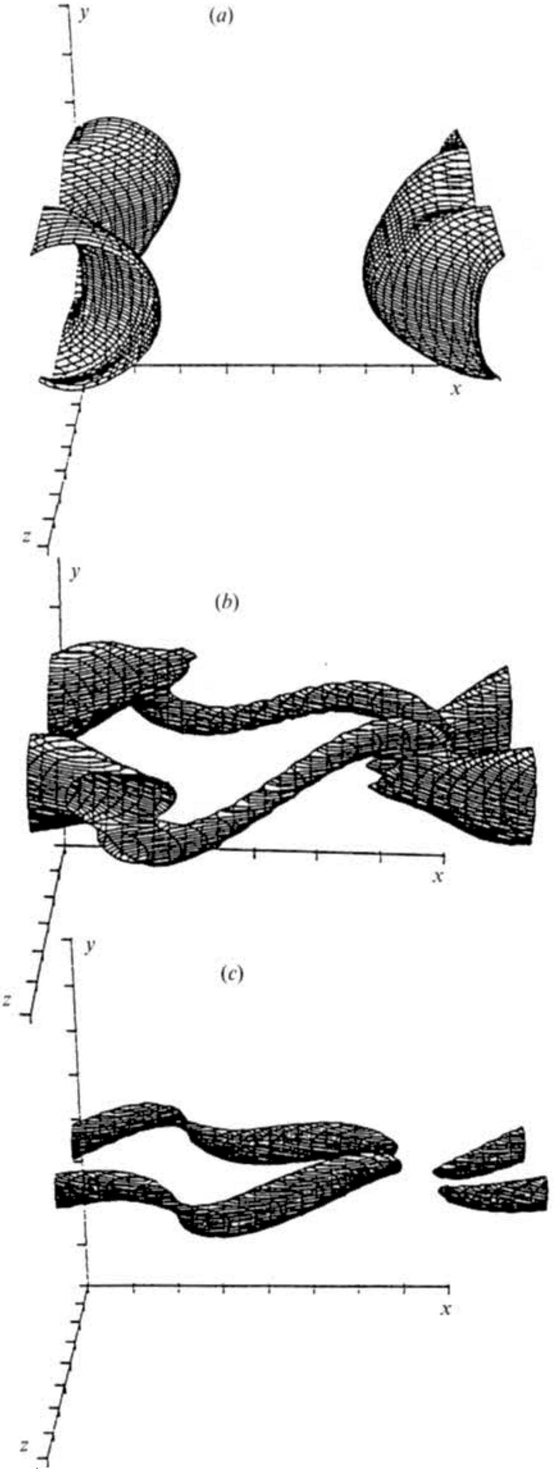

FIGURE 11. Surface of constant pressure showing the large-scale structure developing at (*a*) $M_c = 0.4$, (*b*) $M_c = 0.8$ and (*c*) $M_c = 1.05$.

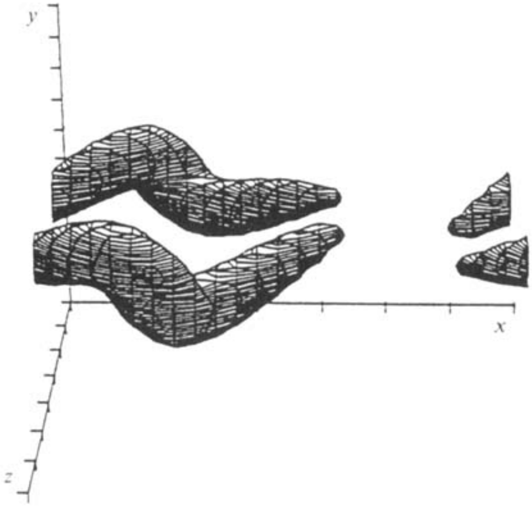

FIGURE 12. Surface of constant pressure showing the structure developing at $M_c = 0.8$ with the phase $\phi = 0$.

The important conclusion from the plots of mode energy is that the general behaviour observed in the linear region of disturbance growth extends into the nonlinear region. The relative importance of two-dimensional and oblique waves, as predicted by linear stability theory, is also found in the nonlinear region. Dominance of oblique waves at the high Mach number $M_c = 1.05$ is found in the nonlinear simulation as well as in the linear stability calculation.

As described in the previous section, we can identify low-pressure regions in the flow with strong rotation. Therefore, pressure is a good method to identify large-scale structure. Perspective views of a surface of constant pressure, that encloses a region of strong rotation, are shown on figure 11 (*a–c*) for the flow field at the ends of the simulations at $M_c = 0.4$, 0.8 and 1.05 respectively. At $M_c = 0.4$ (figure 11 *a*) we find the translative mode of secondary instability, as discussed in the previous section. At $M_c = 0.8$ (figure 11 *b*) we find a weakening of the spanwise structure, which develops a larger amplitude of spanwise oscillation. We also find the development of oblique inclined vortices in the region between two spanwise rollers, where at low Mach number the streamwise 'braid' vortices formed. By $M_c = 1.05$ (figure 11 *c*) we find that the influence of the two-dimensional instability has nearly disappeared, and we are left with a pattern of four regions of rotating fluid. There is one pair of equal and opposite oblique vortices at the streamwise location $x = 0$, where at low Mach number the spanwise roller formed, and another pair at the streamwise location $x = \frac{1}{2}L_x$, where at low Mach number the braid vortices formed. This high-Mach-number structure will be examined in more detail in the next section.

It is noted that no shock waves formed in any of our three-dimensional simulations, even when the free-stream Mach number was supersonic ($M_c = M_1 = 1.05$). Simulations with comparable Reynolds numbers in two-dimensions always developed shocks above $M_c \approx 0.7$. It appears that, when given the freedom to evolve in three dimensions, the mixing layer develops a structure without shock waves.

The strong three-dimensionality observed in our simulations suggests a possible limitation of the simple model of the compressible mixing layer (Papamoschou & Roshko 1988). The model assumes a two-dimensional topological picture of the flow, with isentropic flow from the free streams to a stagnation point. Shock waves must

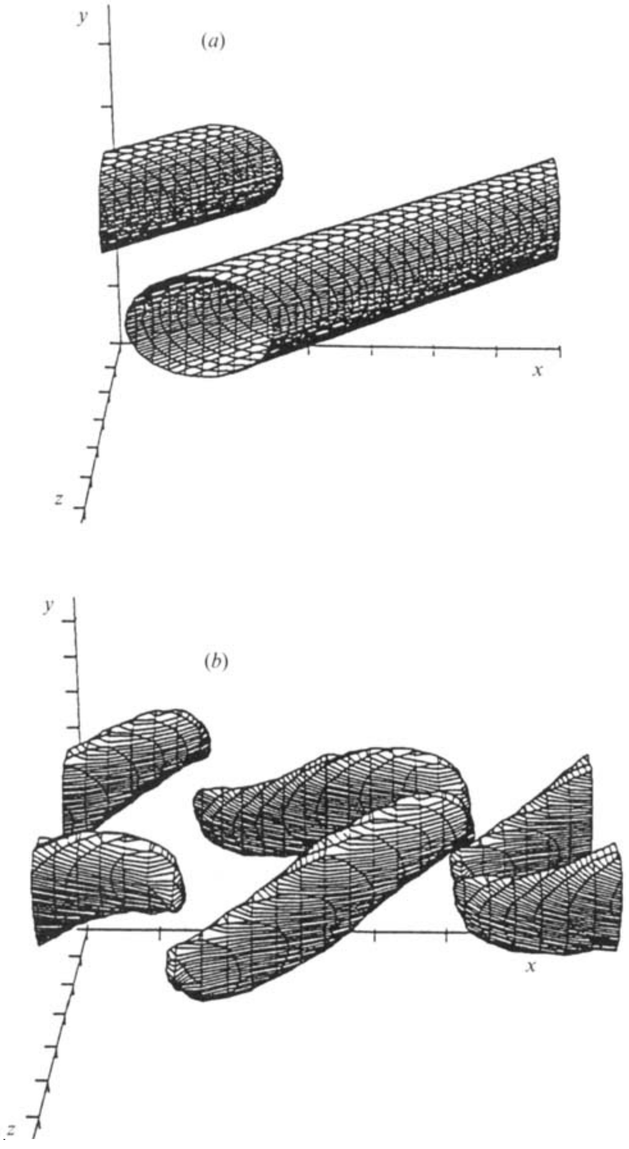

FIGURE 13. Surface of constant pressure showing model structures developing at $M_c = 0.8$ from (*a*) a single oblique instability wave and (*b*) a pair of equal and opposite oblique instability waves.

then be incorporated into the model to explain measurements of convective velocity (Papamoschou 1989). It is speculated that in three dimensions the flow topology changes so that stagnation points are reached without the necessity of shock waves.

To complete this section we consider the effect of phase at the intermediate Mach number $M_c = 0.8$. The alternative phase is $\phi = 0$, which gave the slightly unstable 'bulging' mode of secondary instability at low Mach number. The developed structure from a simulation with $\phi = 0$ (but with otherwise identical conditions to the above) is shown by means of a pressure surface on figure 12. The developed structure is different in detail, though just as three-dimensional as the structure which developed with $\phi = \frac{1}{2}\pi$. Whilst it would be preferable to simulate many different phases between 0 and 2π, it is felt that simulations with $\phi = 0$ and $\phi = \frac{1}{2}\pi$

give the essential phase effects, representing the two cases of streamwise vorticity initially in or out of phase with the spanwise roller. The trend toward obliquely oriented vortical regions is clear. At convective Mach numbers $M_c > 1$ the two-dimensional wave is so weakly amplified that its phase will have little effect.

5.3. *Structure at high Mach number*

Using results from previous sections, we can make some predictions about the kind of large-scale structures which may develop out of flow instabilities in the mixing layer at high Mach number. We consider especially the region $M_c > 1$, where the oblique instability waves are dominant. The kind of picture which may emerge from background noise was shown on figure 6(*c*) for $M_c = 1.05$. There were observed to be regions where one oblique wave dominated, and regions where the addition of two opposite oblique waves was important. To investigate the further development of such wave combinations, simulations were made of a single oblique wave and of a combination of equal and opposite oblique waves. A Mach number of $M_c = 0.8$ was selected so that a lower Reynolds number $Re = 400$ could be used, in order to get further into the nonlinear development before running into resolution problems. Other parameters were chosen to be the same as for the $M_c = 0.8$ simulation in the previous section. Results from this section are expected to apply to the higher-Mach-number regime $M_c > 1$, where more oblique waves are more unstable.

The developed structure arising from a single oblique wave is, not surprisingly, a single oblique vortex. The structure developing from two equal and opposite oblique waves is more complex. Pressure surfaces at the final time in the simulations are shown on figure 13(*a*, *b*) for the two cases. The structure developing from the pair of equal and opposite oblique instability waves (figure 13*b*) contains four main regions of rotating fluid. At $x = 0$ there are two counter-rotating vortices, inclined in y relative to the x-axis, and oblique in z relative to the x-axis. There are two more vortices at $x = \frac{1}{2}L_x$, similar to those at $x = 0$, but with the opposite sense of ω_x rotation. Each of the pairs of oblique vortices can be considered similar to the Λ-structures in transitional boundary-layer flow. The induced motion of each leg on the other gives the inclined nature of the vortices. The vortices become more inclined as the simulation proceeds. The rotation at the heads of the Λ-structures is weak, and there is no suggestion of rotation of the head of one Λ-structure around the tail of the (inverted) Λ-structure beneath it. The structure can be thought of as two vortex lines, passing through the peaks of vorticity. One line passes through the vortices at $x = 0$, $z = \frac{1}{4}L_z$ and $\frac{3}{4}L_z$, and the other passes through the vortices at $x = \frac{1}{2}L_x$, $z = \frac{1}{4}L_z$ and $\frac{3}{4}L_z$. The periodicity means that both vortex lines zigzag *ad infinitum* in the spanwise direction. Perspective and top views of these vortex lines are shown on figure 14. The vortex lines are staggered in the streamwise direction, similar to the staggered Λ-vortices observed in boundary-layer transition (Herbert 1988). However, the boundary-layer case is a subharmonic secondary instability, whereas the case described here is a fundamental *primary* instability.

The scalar field for the structure resulting from two equal and opposite oblique waves is especially rich in detail. The scalar (or mixture fraction) f was originally specified by a hyperbolic tangent profile, and tags fluid from the free streams with a value of 0 (lower stream) or 1 (upper stream). We shall plot contours of the quantity $f-0.5$, with negative contours shown with dashed lines in order to clearly distinguish between fluid from each side of the mixing layer. Thus, solid contours show fluid that originated on the upper side, and dashed contours show fluid that originated on the lower side. A cut through the (x, z) plane at $y = 0$ is shown on figure 15(*a*). The four

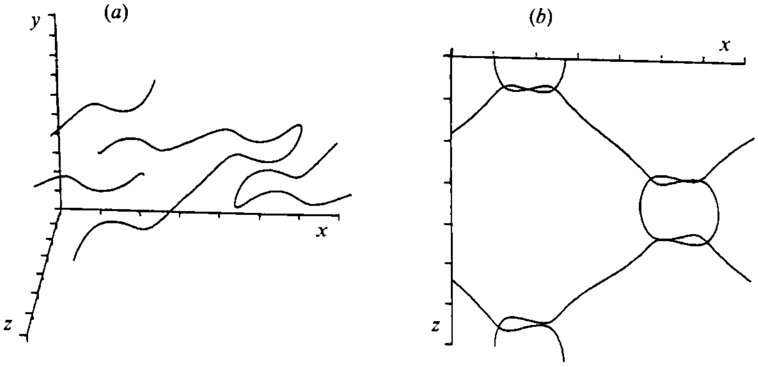

FIGURE 14. Vortex lines passing through the vortex cores for the structure developing from a pair of equal and opposite oblique instability waves at $M_c = 0.8$: (*a*) perspective view and (*b*) top view.

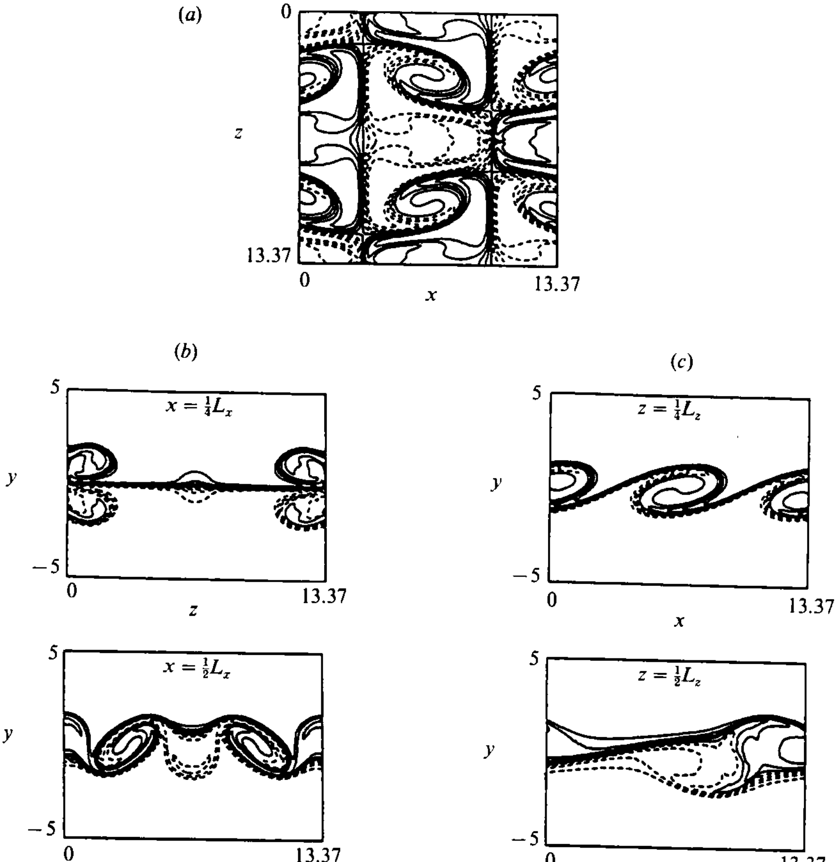

FIGURE 15. Cuts through the scalar field of the structure developing from a pair of equal and opposite oblique instability waves at $M_c = 0.8$: (*a*) (x, z)-plane at $y = 0$, (*b*) (y, z)-plane at $x = \frac{1}{4}L_x/4$ and $x = \frac{1}{2}L_x$, and (*c*) (x, y)-plane at $z = \frac{1}{4}L_z$ and $z = \frac{1}{2}L_z$.

main rotational regions show clearly. The regions of strong scalar gradient at $x = \frac{1}{4}L_x$ and $\frac{3}{4}L_x$, $z = \frac{1}{4}L_z$ and $\frac{3}{4}L_z$ are complex three-dimensional saddle points, where fluid from the free streams is brought to rest, and high pressure ensues. Cuts through the scalar in the (y, z)-plane at $x = \frac{1}{4}L_x$ and $x = \frac{1}{2}L_x$ are shown on figure 15(*b*). Mushroom-

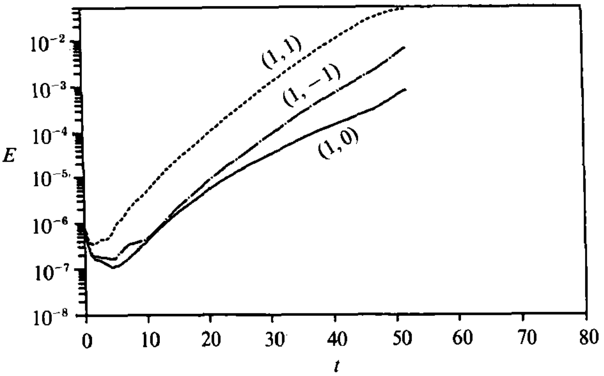

FIGURE 16. Plot of energy E of modes (1,0), (1,1) and (1, −1) versus time for simulation beginning with random noise at $M_c = 0.8$.

shaped structures are found at the plane $x = \frac{1}{2}L_x$ due to the counter-rotating nature of the vortices. Cuts through the (x,y) plane of the scalar at $z = \frac{1}{4}L_z$ and $z = \frac{1}{2}L_z$ are shown on figure 15(c). The cut at $z = \frac{1}{4}L_z$ might at first glance appear similar to the two-dimensional roller structure at low Mach numbers. Only examination of the other planar cuts reveals the highly three-dimensional structure of the flow field. This effect has been clearly demonstrated experimentally by Clemens *et al.* (1990). They studied a mixing layer at $M_c = 0.6$ and showed how schlieren photography could give an illusion of two-dimensionality, when in reality the flow field was highly three-dimensional.

The probability density function (p.d.f.) of the scalar is of much interest in combustion applications (see e.g. Mungal & Dimotakis 1984). Our simulations do not contain the small-scale eddies that are responsible for much of the mixing beyond the mixing transition. However, it is possible to make some limited inferences, based on the observed large-scale structure. In particular, the inclined nature of the Λ-vortices seems to make it possible for fluid to be locally mixed at some level other than that associated with the overall entrainment ratio. The heads of the Λ-vortices exist largely in one or other of the free streams, and may be expected to contain more fluid from that side of the mixing layer. The overall scalar p.d.f. would then have a lower peak at the entrainment ratio. It is unfortunately not possible from these simulations to quantify this effect.

5.4. *Simulation with random initial conditions*

In this section we present results from a simulation conducted to check the generality of the findings of the previous sections. In particular, we would like to break the symmetry that was imposed by the choice of equal and opposite oblique waves. To do this, and to remove other possible biases, random noise was chosen as the initial condition. Unfortunately, numerical limitations prevent us from carrying the random noise simulations of §4, into the nonlinear regime. Therefore, the same restricted domain as for the forced simulations of §§5.2 and 5.3 was used. Random noise was added to the mean flow in the manner of (15), with an amplitude $a = 0.025$. The intermediate-Mach-number case $M_c = 0.8$ was chosen for simulation, and other parameters were chosen to be the same as for the simulation at this Mach number in §5.2.

Figure 16 shows how the linearly unstable waves grow out of the random noise initial condition. This process appears to take about 5 time units. Clearly the extent

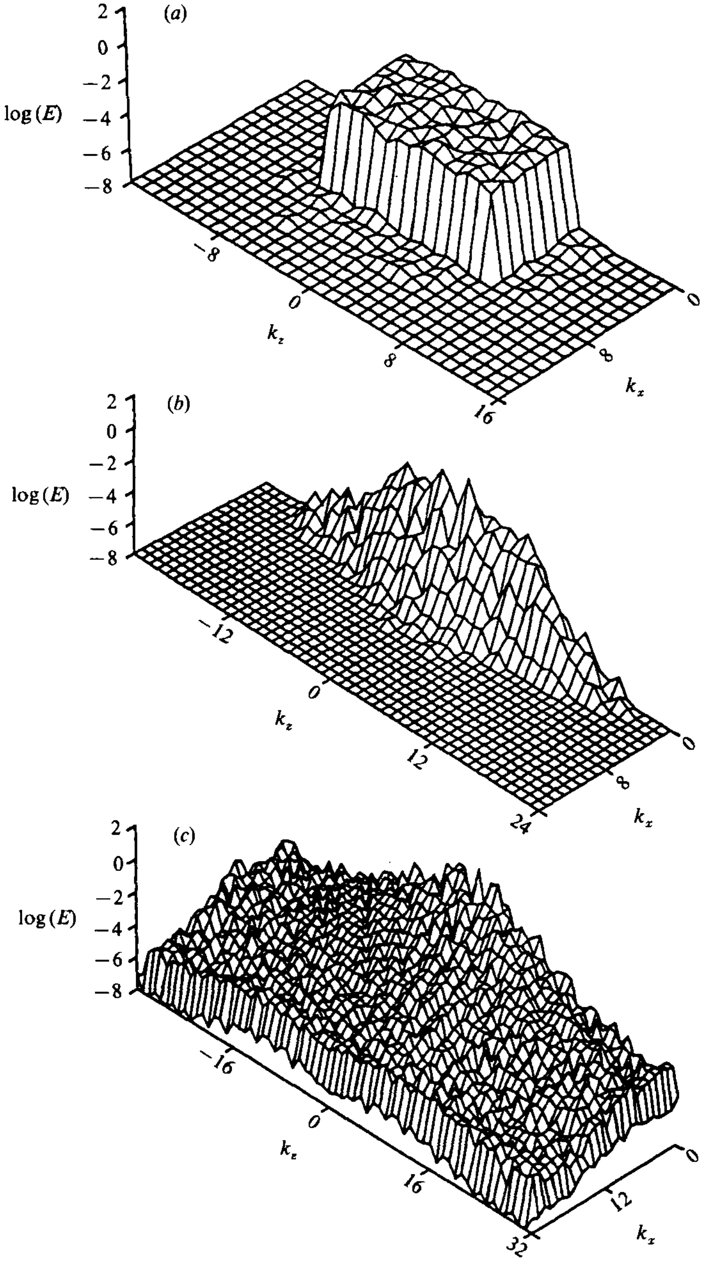

FIGURE 17. Two-dimensional energy spectrum $E(k_x, k_z)$ for the simulation starting with random noise at $M_c = 0.8$: (*a*) $t = 0$, (*b*) $t = 29.6$, and (*c*) $t = 52.0$.

to which different unstable modes are energized will depend upon the initial random number seed. For this particular case it is apparent that the two-dimensional (1,0) mode is only weakly energized, and that the oblique (1,1) mode is more strongly energized than the (1, −1) mode. The symmetry between the oblique modes has been broken.

We observe the progress of this simulation by making a carpet plot of the energy content $E(k_x, k_z)$ for all the waves in the simulation, and by plotting an (x, z)-cross-

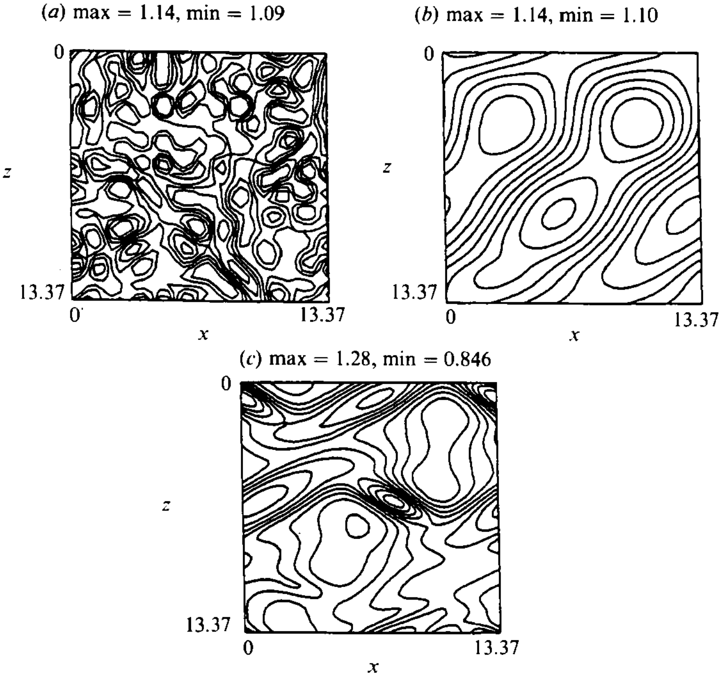
(a) max = 1.14, min = 1.09

(b) max = 1.14, min = 1.10

(c) max = 1.28, min = 0.846

FIGURE 18. Planar (x, z) cuts through the pressure field at $y = 0$ showing organized structure developing from random noise: (a) $t = 0$, (b) $t = 29.6$, and (c) $t = 52.0$.

section through the pressure field at $y = 0$. These plots are made at times $t = 0$, 29.6 and 52.0 and shown on figures 17 and 18 respectively. The initial carpet plot of mode energies (figure 17*a*) is flat owing to the flat spectrum of the random noise. By time $t = 29.6$ (figure 17*b*) the low-frequency linearly unstable waves have been amplified and the high-frequency waves have been damped. The high-frequency component at this time is partially a remnant of the original random noise, and partially due to the high-frequency Fourier modes needed to resolve the developing large-scale structure. At the final time (figure 17*c*) we observe that the spectrum has filled out completely.

The pressure sequence on figure 18 shows the development of organized large-scale structure in the flow. Initially (figure 18*a*) we have just random noise. At $t = 29.6$ (figure 18*b*) we see that structure is developing from the instabilities, with one of the oblique waves clearly in evidence. At the final time $t = 52.0$ (figure 18*c*) we see localized regions of low pressure, associated with the strongly rotating parts of the large-scale structure.

The developed structure is perhaps best observed on a plot of a three-dimensional surface of constant pressure, as done in previous sections. This is shown on figure 19. The similarities with figures 11(*b*) and 13(*b*) are striking. We again have four regions of strong rotation, and these regions are inclined and oblique. The picture is most similar to the case in figure 13(*b*), where the structure developed from a pair of oblique waves, with no two-dimensional forcing. This is consistent with our observation that the two-dimensional wave was not strongly energized by the random number seed of this simulation. More surprising perhaps is that we do not see a dominance of one oblique wave over the over, even though they were energized differently. The structure is much closer to figure 13(*b*) than to figure 13(*a*). This adds additional weight to the structure in figure 13(*b*) being a representative large-scale

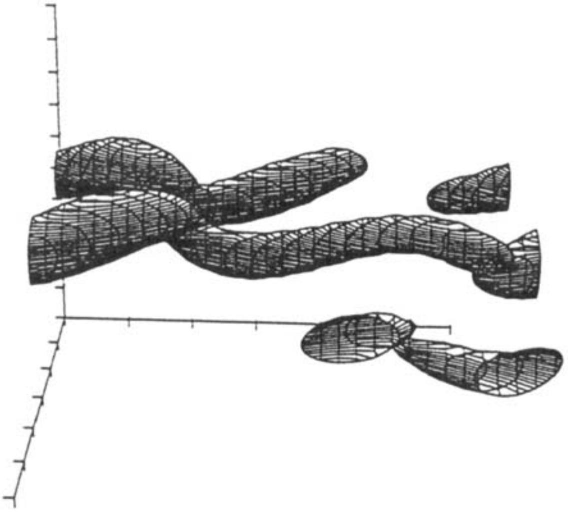

FIGURE 19. Surface of constant pressure showing the large-scale structure that developed from random noise initial conditions at $M_c = 0.8$.

structure for the high-Mach-number mixing layer. One feature of experiments that may be important is that an oblique instability wave can reflect off the sidewalls. In this situation a wave may interact with itself, and thus tend to be more like our simulation of two equal and opposite oblique waves.

Some comment is in order on the apparent 'cleanliness' of the simulations presented in this paper. The simulation presented in this section shows that the smoothness of the final pressure surfaces is due to the dominance of the primary instability in the flow, and not just because we impose clean initial conditions. In the later stages of the development of this flow, which unfortunately cannot be simulated at present, we would expect to find secondary instabilities developing on top of the structure of figure 13(*b*). Eventually we would expect some kind of mixing transition (generation of small eddies and hence high mixing) taking place, similar to incompressible free shear flows. What we feel is important in a flow like the mixing layer, which is dominated by a strong inflexional instability, is that the instability process continues in the fully developed turbulent regime, and the same structure will continually reimpose itself at the largest scales. Thus, although we have only simulated the initial steps in the transition process, we believe the final large-scale structure would be similar in the fully developed turbulent state.

6. Conclusions

Three-dimensional direct numerical simulations of the full compressible Navier–Stokes equations have been presented. A combination of spectral and high-order accurate finite-difference methods was used to achieve high spatial resolution.

Simulations of the linear region of disturbance growth, using random noise as the initial condition, confirmed some earlier linear stability results. Oblique waves were found to be the most rapidly amplified instabilities for convective Mach numbers above 0.6. No evidence was found for any other unstable waves, besides those already known from the linear stability analysis.

At low Mach number ($M_c = 0.4$) we were able to reproduce the incompressible secondary instability characteristics of Pierrehumbert & Widnall (1982). Specifically, by choosing the phase of a two-dimensional instability wave relative to a pair of equal and opposite oblique waves, the 'bulging' and 'translative' modes of secondary instability were found. In agreement with Pierrehumbert & Widnall we found strong instability only with the translative mode.

Using a fixed combination of instability waves (a two-dimensional wave and a pair of equal and opposite oblique waves, with phase fixed to give the translative mode of secondary instability) the effect of Mach number was investigated. A change was observed in the large-scale structure that develops in the nonlinear stage of instability growth. The low-Mach-number structure of a strong two-dimensional roller, with streamwise 'braid' vortices in between, disappeared at higher Mach numbers. Strong oblique and inclined regions of rotation were found at the higher Mach numbers of $M_c = 0.8$ and 1.05. The nonlinear growth of instabilities followed the linear trends, with oblique modes dominant in the nonlinear evolution at high Mach number.

No shock waves were found in these three-dimensional simulations, even at Mach numbers where shock waves did form in comparable two-dimensional simulations. Whilst it is not possible to say that there will never be shock waves, it does appear that the flow topology is able to change in a three-dimensional manner at the higher Mach numbers to make shock waves unnecessary.

Model large-scale structures for the mixing layer at high Mach numbers ($M_c > 1$) were proposed, based on the nonlinear development of a single oblique wave, or a pair of equal and opposite oblique waves. The former gives a single oblique vortex, while the latter yields a complex three-dimensional structure that can be thought of as a pair of Λ-vortices, staggered in the streamwise direction. A simulation with purely random initial conditions gave a structure very similar to the model structure developing from a pair of equal and opposite oblique waves.

There are several implications from our work that warrant further investigation. The change in large-scale structure found at high Mach numbers may lead to different mixing characteristics at high Mach numbers. In particular, it is considered possible that the scalar probability density function will have a different form at higher Mach numbers. Also, there must be some kind of subharmonic merging process at the higher Mach numbers; an analogue to the low-Mach-number two-dimensional 'pairing' process must exist for the complex double-Λ structures.

The authors would like to thank S. Lele for help with the numerical method. M. G. Mungal, P. Moin and N. N. Mansour contributed useful suggestions. This work was performed at Stanford University with the financial support of the US Air Force Office of Scientific Research, under Contract F49620-86-K-0022. Computational facilities were provided by the NASA-Ames Research Center. This support is gratefully acknowledged.

REFERENCES

ANDERSON, D. A., TANNEHILL, J. C. & PLETCHER, R. H. 1984 *Computational Fluid Mechanics and Heat Transfer*. McGraw-Hill.

BERNAL, L. P. & ROSHKO, A. 1986 Streamwise vortex structure in plane mixing layers. *J. Fluid Mech.* **170**, 499–525.

BIRCH, S. F. & EGGERS, J. M. 1973 A critical review of the experimental data for developed free turbulent shear layers. *NASA SP*-321, pp. 11–40.

BOGDANOFF, D. W. 1983 Compressibility effects in turbulent shear layers. *AIAA J.* **21**, 926–927.

Brown, G. L. & Roshko, A. 1974 On density effects and large scale structure in turbulent mixing layers. *J. Fluid Mech.* **64**, 775–816.

Clemens, N. T. & Mungal, M. G. 1990 Two- and three-dimensional effects in the supersonic mixing layer. *AIAA/ASME/SAE/ASEE 26th Joint Propulsion Conf. July 1990, Orlando, Florida, AIAA Paper* 90–1978.

Clemens, N. T., Mungal, M. G., Berger, T. E. & Vandsburger, U. 1990 Visualizations of the structure of the turbulent mixing layer under compressible conditions. *AIAA Paper* 90–0500.

Eberhardt, S., Riley, J. J., Soetrisno, M. & Greenough, J. A. 1988 A numerical study of inviscid, supersonic mixing layers. *Intl Workshop on the Physics of Compressible Turbulent Mixing, Princeton, Oct. 1988.*

Greenough, J., Riley, J., Soetrisno, M. & Eberhardt, D. 1989 The effects of walls on a compressible mixing layer. *AIAA Paper* 89–0372.

Gropengiesser, H. 1969 Beitrag zur Stabilität freier Grenzschichten in kompressiblen Medien. *DLR FB* 69–25. (English transl. *NASA TT* F-12,786, 1970.)

Herbert, T. 1988 Secondary instability of boundary layers. *Ann. Rev. Fluid Mech.* **20**, 487–526.

Lele, S. 1989 Direct numerical simulation of compressible free shear flows. *AIAA Paper* 89–0374.

Lele, S. 1990 Compact finite difference schemes with spectral-like resolution. *CTR Manuscript* 107. Center for Turbulence Research, Stanford University, CA. (Submitted to *J. Comput. Phys.*)

Lessen, M. Fox, J. A. & Zien, H. M. 1965 On the inviscid stability of the laminar mixing of two parallel streams of a compressible fluid. *J. Fluid Mech.* **23**, 355–367.

Lessen, M. Fox, J. A. & Zien, H. M. 1966 Stability of the laminar mixing of two parallel streams with respect to supersonic disturbances. *J. Fluid Mech.* **25**, 737–742.

Lin, S. J. & Corcos, G. M. 1984 The mixing layer: deterministic models of a turbulent flow. Part 3. The effect of plane strain on the dynamics of streamwise vortices. *J. Fluid Mech.* **141**, 139–178.

Mack, L. M. 1984 Boundary-layer stability theory. *Special Course on Stability and Transition of Laminar Flow, AGARD Rep.* 709, 3–1 to 3–81.

Mungal, M. G. & Dimotakis, P. E. 1984 Mixing and combustion with low heat release in a turbulent shear layer. *J. Fluid Mech.* **148**, 349–382.

Mungal, M. G. & Hollingsworth, D. K. 1989 Organized motion in a very high Reynolds number jet. *Phys. Fluids* A **1**, 1615–1623.

Papamoschou, D. 1989 Structure of the compressible turbulent shear layer. *AIAA Paper* 89–0126.

Papamoschou, D. & Roshko, A. 1986 Observations of supersonic free shear layers. *AIAA Paper* 86–0162.

Papamoschou, D. & Roshko, A. 1988 The compressible turbulent mixing layer: an experimental study. *J. Fluid Mech.* **197**, 453–477.

Pierrehumbert, R. T. & Widnall, S. E. 1982 The two- and three-dimensional instabilities of a spatially periodic shear layer. *J. Fluid Mech.* **114**, 59–62.

Ragab, S. A. & Wu, J. L. 1988 Instabilities in the free shear layer formed by two supersonic streams. *AIAA Paper* 88–0038.

Rogers, M. M. & Moser, R. D. 1989 The development of three-dimensional temporally-evolving mixing layers. *Seventh Symp. on Turbulent Shear Flows, Stanford, CA, August 21–23, 1989.*

Sandham, N. D. & Reynolds, W. C. 1989 A numerical investigation of the compressible mixing layer. *Rep.* TF-45. Thermosciences Division, Mechanical Engineering Department, Stanford University.

Sandham, N. D. & Reynolds, W. C. 1990 Compressible mixing layer: linear theory and direct simulation. *AIAA J.* **28**, 618–624.

Sandham, N. D. & Yee, H. C. 1989 A numerical study of a class of TVD schemes for compressible mixing layers. *NASA TM*-102194.

Thompson, K. W. 1987 Time dependent boundary conditions for hyperbolic systems. *J. Comput. Phys.* **68**, 1–24.

White, F. M. 1974 *Viscous Fluid Flow*. McGraw-Hill.

WRAY, A. A. 1986 Very low storage time-advancement schemes. *Internal Rep.* NASA-Ames Research Center, Moffett Field, California.

ZHUANG, M., DIMOTAKIS, P. & KUBOTA, T. 1990 The effect of walls on a spatially growing supersonic shear layer. *Phys. Fluids* A **2**, 599–604.